

---

*This copy is for your personal, non-commercial use only.*

---

**If you wish to distribute this article to others**, you can order high-quality copies for your colleagues, clients, or customers by [clicking here](#).

**Permission to republish or repurpose articles or portions of articles** can be obtained by following the guidelines [here](#).

**The following resources related to this article are available online at [www.sciencemag.org](http://www.sciencemag.org) (this information is current as of September 3, 2015 ):**

**Updated information and services**, including high-resolution figures, can be found in the online version of this article at:

<http://www.sciencemag.org/content/349/6252/1080.full.html>

**Supporting Online Material** can be found at:

<http://www.sciencemag.org/content/suppl/2015/09/02/349.6252.1080.DC1.html>

A list of selected additional articles on the Science Web sites **related to this article** can be found at:

<http://www.sciencemag.org/content/349/6252/1080.full.html#related>

This article **cites 27 articles**, 2 of which can be accessed free:

<http://www.sciencemag.org/content/349/6252/1080.full.html#ref-list-1>

This article has been **cited by** 1 articles hosted by HighWire Press; see:

<http://www.sciencemag.org/content/349/6252/1080.full.html#related-urls>

This article appears in the following **subject collections**:

Materials Science

[http://www.sciencemag.org/cgi/collection/mat\\_sci](http://www.sciencemag.org/cgi/collection/mat_sci)

## METALLURGY

# Linear complexions: Confined chemical and structural states at dislocations

M. Kuzmina, M. Herbig, D. Ponge, S. Sandlöbes, D. Raabe\*

For 5000 years, metals have been mankind's most essential materials owing to their ductility and strength. Linear defects called dislocations carry atomic shear steps, enabling their formability. We report chemical and structural states confined at dislocations. In a body-centered cubic Fe–9 atomic percent Mn alloy, we found Mn segregation at dislocation cores during heating, followed by formation of face-centered cubic regions but no further growth. The regions are in equilibrium with the matrix and remain confined to the dislocation cores with coherent interfaces. The phenomenon resembles interface-stabilized structural states called complexions. A cubic meter of strained alloy contains up to a light year of dislocation length, suggesting that linear complexions could provide opportunities to nanostructure alloys via segregation and confined structural states.

Structural defects such as interfaces or dislocations in crystalline solid solutions are disturbed regions and attract solute segregation when diffusion is enabled (1–5). According to the Gibbs isotherm, the driving force is the reduction of the system's energy. Extending this concept also to nonisostructural cases suggests that local structural transformations can occur if the chemical composition and stress at a defect reach a level sufficient for stabilizing a state different from that of the matrix (6, 7). The concept of interface complexions (8–17) extends the classical isotherm to interface-stabilized states that have a structure and composition different from that of the matrix and remain confined in the region where they form. We observed such a phenomenon also at linear defects—edge dislocations—in a binary Fe–9 atomic % Mn model alloy in which a stable face-centered cubic (fcc; austenitic) confined structure forms in an otherwise body-centered cubic (bcc; martensitic) crystal. This is a phenomenological one-dimensional (1D) analog of the previously observed complexions that were observed at planar defects (8).

We homogenized the Fe–9 atomic % Mn alloy at 1100°C and then quenched and cold-rolled it to 50% reduction for increasing the dislocation density. Subsequent annealing at (i) 400°C for 336 hours (2 weeks); (ii) 450°C for 6 hours, 18 hours, and 336 hours; and (iii) 540°C for 6 hours enabled Mn diffusion (18). To characterize structure and composition at the same positions, we conducted correlative scanning transmission electron microscopy–atom probe tomography (STEM-APT) analysis (19–23). We identified structural defects using STEM and cross-correlated it with solute decoration observed with APT (Fig. 1).

Two grain boundaries and a single dislocation line are highlighted in Fig. 1 by blue arrows in the STEM micrograph and in the 3D atom map, in which they are visible as Mn-enriched regions. The correlative STEM experiments clearly identify the linear Mn-enriched features in the APT volumes as dislocations. As evident from the STEM micrograph, not all dislocations attract solute segregation high enough to be detectable with APT (Fig. 1A, red arrow “1”).

We obtained 1D compositional profiles along cylindrical regions with 1 nm diameter at individual locations (Fig. 1E). Profile 1 shows a concentration of  $25 \pm 2$  atomic % Mn at the dislocation core, which corresponds to an enrichment factor of 2.7 compared with the matrix concentration of Mn (9.1 atomic %). The average thickness of the Mn-enriched zone is ~1 nm. Besides the high Mn content at the dislocation cores, the composition along the dislocation line (profile 2) reveals periodic Mn changes—enriched and depleted zones alternating with a spacing of ~5 nm, resembling a nano-sized pearl necklace.

Sufficient segregation in conjunction with local elastic distortion at the defect may promote formation of confined structural states. This phenomenon has been observed at grain boundaries in Fe–Mn alloys and was explained in terms of a conventional phase transformation model (6, 7). The huge segregation level observed here at some of the dislocations reveals similar features, reaching up to 25 atomic % Mn. This is in excellent agreement with the equilibrium concentration of Mn in the fcc phase (austenite) in the bcc–fcc two-phase region of the binary Fe–Mn system at the given annealing temperature (450°C), indicating an austenitic state of the dislocation core region. We conducted experiments on three samples, exposed to different annealing temperatures (400°C, 450°C, and 540°C) to study this further. We quantified the average compositional

profiles around all probed dislocations observed in all individual APT data sets using proximity histograms (“proxigrams”) (Fig. 2) (24). For all temperatures, we found an excellent agreement of the thermodynamically predicted equilibrium Mn concentrations (18) in austenite (dashed lines), with the experimentally observed local chemical compositions within 0.5 to 1 nm distance from the dislocation core.

As a third approach to prove that the dislocation cores transform from bcc to fcc, we performed transmission electron microscopy (TEM) to reveal the local crystallographic structures at the Mn-enriched dislocation sections. The investigations were done on martensite grains tilted a few degrees away from the [001] zone axis. Because of the small volume of the Mn-enriched dislocation core regions with respect to the surrounding matrix, no fcc reflections are visible in the diffraction patterns (Fig. 3A). Nevertheless, the measured area contains fcc regions that fulfill a Kurdjumov-Sachs (K-S) or Nishiyama-Wassermann (N-W) orientation relationship with the parent bcc grain, as we demonstrated by means of dark-field imaging. Shown in Fig. 3A is the diffraction pattern taken from a region containing a small-angle grain boundary (Fig. 3B). The diffraction pattern is indexed as  $[001]_{\text{bcc}}$ ; the positions of the fcc diffraction spots for a N-W orientation relationship are also plotted into the same image. Austenite with a K-S orientation relationship is rotated by  $5.26^\circ$  around  $[011]_{\text{bcc}}$  and the corresponding reflections are within the yellow circle in Fig. 3A. For better clarity, only one N-W fcc variant is shown, but the symmetric relationship applies for all possible variants. The bright-field TEM micrographs (Fig. 3B) show a mixed-type small-angle grain boundary containing edge and screw dislocations. When performing dark-field imaging using the yellow region in Fig. 3A, only the edge dislocations produce contrast. As clearly visible from the diffraction pattern (Fig. 3A), bcc dislocations would not give contrast under these dark-field diffraction conditions. These TEM results are a direct proof of the presence of a confined zone, with fcc structure having a K-S or N-W orientation relationship with respect to the martensitic matrix at edge dislocations.

Although these experiments give proof of austenitic states at the edge dislocation cores, to our surprise we did not detect any further growth of these regions into the martensite matrix, even during extended annealing treatments (18). In classical nucleation theory, a newly formed phase will grow once it has overcome the nucleation barrier. However, the analysis of samples annealed even for 2 weeks (336 hours) at 450°C in the two-phase region of the phase diagram revealed no change in size or composition of the austenitic dislocation cores as compared with those of the samples annealed for 6 hours at 450°C (18). This result indicates that these austenitic states are not viable outside of the dislocation core regions, hence matching the confinement characteristic of a complexion.

We further analyzed this phenomenon by use of a thermodynamic energy balance model (25).

Max-Planck Institut für Eisenforschung, Max-Planck-Straße 1, D-40237 Düsseldorf, Germany.

\*Corresponding author. E-mail: raabe@mpie.de

We considered two cases: (i) an incoherent fcc-bcc interface formed by a diffusive transformation and (ii) a coherent interface formed by an athermal reversed Bain transformation from bcc to fcc (displacive transformation) (26). For the second case, the newly formed fcc zone (austenite) should hold an orientation relationship, for which the maximum misfit direction is nearly parallel to the Burgers vector of the dislocation (27, 28). For the case of the incoherent fcc-bcc interface, we considered as an upper bound the removal of the dislocation's strain energy (25); the formation of a new incoherent interface; and a free-energy term associated with the transition from the bcc into the fcc state. For the special case of a coherent, athermal transformation, we added an additional energy penalty term for the misfit distortion associated with the reverse transformation. Including these con-

tributions, we calculated the free energy per unit length of a cylinder surrounding an infinite straight dislocation

$$F = -A \log(r/R) + 2\pi\gamma r - \pi f r^2 [+B\pi r^2] \quad (1)$$

where  $r$  is the spatial coordinate perpendicular to the dislocation line,  $R$  is the inner cut-off radius for the dislocation core ( $\sim b$ ),  $A = [Gb^2/4\pi(1-\nu)]$  is the energy of an edge dislocation ( $G$ , shear modulus;  $b$ , Burgers vector; and  $\nu$ , Poisson ratio),  $\gamma$  is the interfacial energy between the newly formed confined fcc zone and the bcc matrix,  $f = \Delta F_v$  is the bcc-fcc transformation energy, and  $B = Gs^2(2-\nu)/8(1-\nu)$  is the distortion energy for the special case of a displacive transformation ( $s$ , net shear in a plane). The latter term is in brackets because it applies only in the case of a diffusionless transformation from bcc to fcc. The transformation

free energy  $\Delta F_v$  was taken from (18, 29). For the fcc-bcc interface energy ( $\gamma$ ), we used values ranging from  $0.2 \text{ Jm}^{-2}$  for a coherent interface with a specific orientation match, which is expected for the case of a displacive transformation, up to  $1.2 \text{ Jm}^{-2}$  for a less ordered one, which is expected for a diffusive transformation (Fig. 4) (30).

Indications for either a diffusive or displacive transformation mechanism exist. The pronounced partitioning of Mn suggests at first view a diffusional mechanism. However, the initial segregation occurs before the transformation, and the partitioning could go on after a displacive transformation. The crystallographic coherency between the two structures (matrix, bcc; dislocation core, fcc) observed in TEM seems to support a displacive transformation mechanism; however, K-S relationships can occur for diffusive transformations, too.

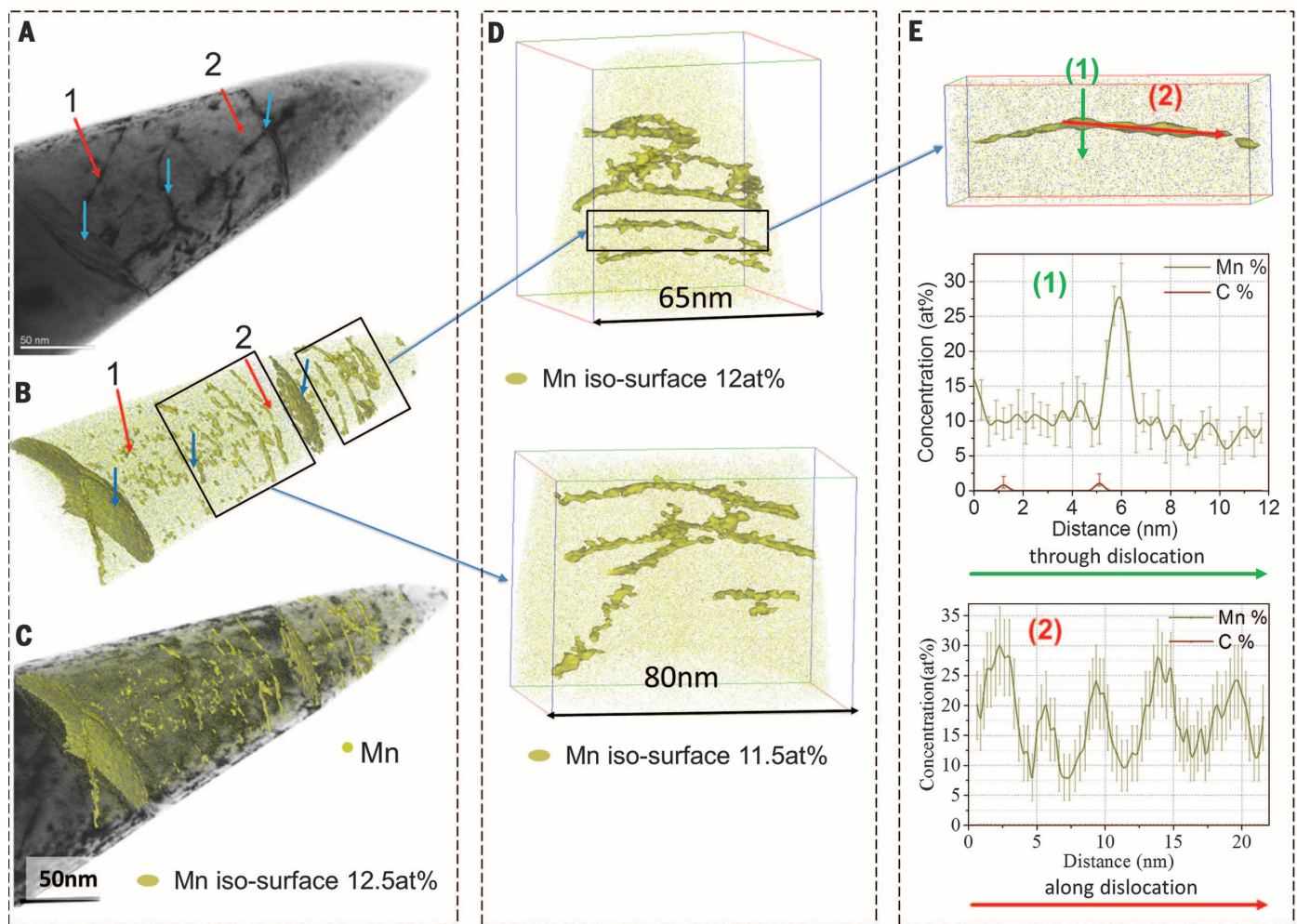


**Fig. 1. Fe-9 atomic % Mn solid solution, 50% cold-rolled and annealed at 450°C for 6 hours to trigger Mn segregation. (A)** Bright-field STEM image. **(B)** Correlative atom probe tomography results of the same tip shown in (A) using 12.5 atomic % Mn isoconcentration surfaces (12.5 atomic % Mn was chosen as a threshold value to highlight Mn-enriched regions). The blue arrows mark grain boundaries and dislocation lines that are visible in both the STEM micrograph and the atom probe tomography map. Not all dislocations visible in STEM are also visible in the atom probe data and vice versa (red arrows). **(C)** Overlay of (A) and (B). **(D)** Magnification of two subregions taken from (B). **(E)** 1D compositional profiles along 1 (perpendicular to dislocation line) and 2 (along dislocation line).

**Fig. 2. Partitioning of Mn among the matrix and the dislocation cores.** Proxigram of the local Mn concentration at dislocation lines in the binary Fe–9 atomic % Mn model alloy, annealed at 400°C for 336 hours (2 weeks) (blue line), 450°C for 6 hours (black line), and 540°C for 6 hours (red line). The parameters used for the isoconcentration surface values and for the proxigram calculations (18) were identical for all data sets (delocalization, 2 nm; voxel size, 0.7 nm; Mn isoconcentration value, 14 atomic % as threshold value). The thermodynamically predicted equilibrium concentrations of Mn in austenite at the respective annealing temperatures are marked by dashed lines (18).

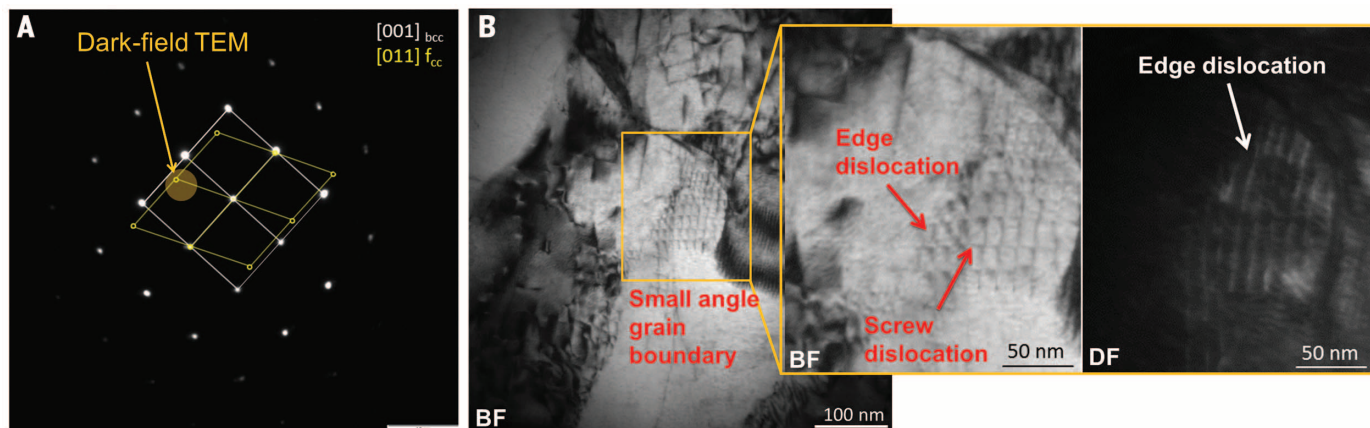
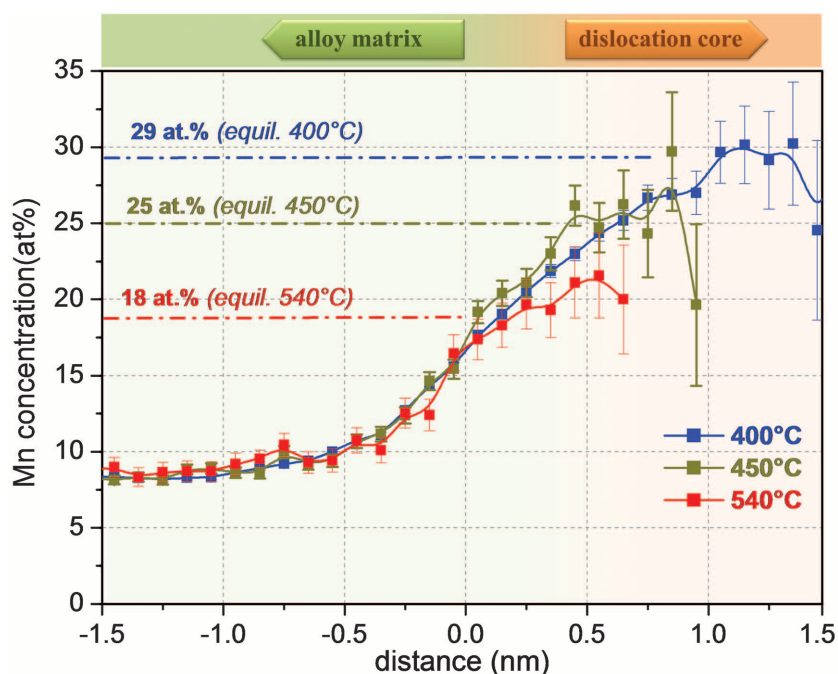


**Fig. 3. Confined austenitic states at dislocation segments in a martensitic matrix imaged with TEM.** (A) Selected area diffraction pattern (SADP) from the enlarged region shown in (B). The diffraction patterns are indexed as  $[001]_{\text{bcc}}$ ; the positions of fcc diffraction spots for a N-W orientation relationship are drawn into the image. (B) BF-TEM and dark-field (DF)-TEM micrographs of a small-angle grain boundary. The DF micrograph was taken from the region marked by the yellow circle in (A), indicating austenitic edge dislocation core regions.

For the case of a displacive confined transformation at a dislocation in conjunction with a coherent fcc-bcc low-energy interface, the energy balance reaches a steep local minimum at an austenite size of  $\sim 0.4$  nm. We interpret this as a stable austenitic state that remains confined to the defect.

The colored curves indicate solutions for a diffusive mechanism in conjunction with an incoherent interface by using different fcc-bcc interface energies. Both types of scenarios could in principal explain our observations (Fig. 4). The activation barrier for such a linear structure to be turned into a conventional phase, when in a two-phase region of the phase diagram, is rath-

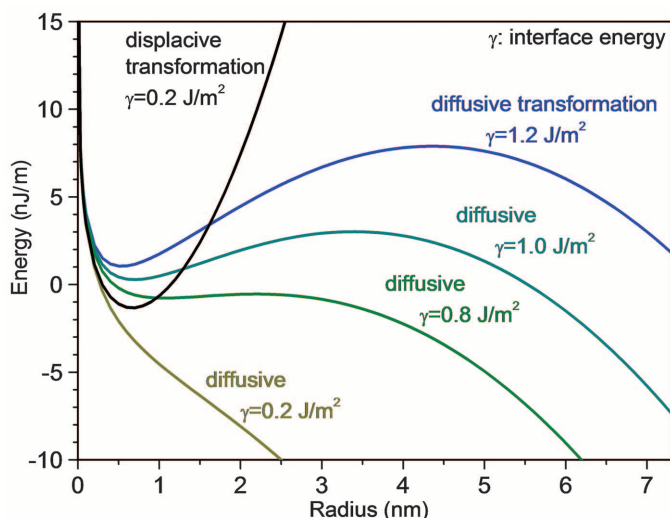
er small for the diffusive cases or—for interface energies  $< 1 \text{ J/m}^2$ —even absent. In such cases, a spontaneous (pseudospinodal) phase formation could occur (31). The coherency between the matrix and the austenitic dislocation core and the fact that these fcc zones remain strictly confined at the defects without any temporal changes in size or composition (18) are the reasons why we use the term “linear complexions” to describe the current phenomena.

We also observed that the segregation of Mn forms alternating regions of high and low Mn concentration along a dislocation line (Fig. 1E). We attribute this necklace-like arrangement of the transformation zones to a Rayleigh insta-

bility, which is driven by the minimization of the interface area and occurs if their wavelength exceeds their circumference, as observed in the present case.

Our results confirm confined austenitic states at martensitic dislocation cores. The observations rest on atomic-scale structural and chemical analysis, thermodynamic calculations, and an analytical model that accounts for the free-energy gain obtained when rendering dislocation cores into undistorted spatially confined austenite zones. We suggest extending the recently introduced planar complexion concept phenomenologically to the linear case. The effect observed fulfills all characteristics of a linear

**Fig. 4. Modeling supports a confined austenitic state at a dislocation core in martensite.** Free energy per unit length of an austenitic (fcc) cylinder in a surrounding Fe–9 atomic % Mn martensite (bcc) matrix formed along an infinite straight-edge dislocation line, calculated for a range of interface energies between 1.2 and 0.2 J/m<sup>2</sup> for the case of a diffusive and a displacive confined transformation,



respectively, at a temperature of 450°C. The black line applies to a displacive transformation at a dislocation in conjunction with a coherent fcc-bcc low-energy interface, and the colored curves indicate solutions for a diffusive transformation in conjunction with an incoherent fcc-bcc interface by using different interface energies. The local minima in several of these curves indicate the size of a confined austenitic (fcc) state.

complexion (8)—namely, equilibrium structural and chemical states through defect stabilization, geometrical confinement to the defect region, individual structural and compositional state, as well as dimensional and compositional stability. The thermodynamic driving forces for the formation of planar and linear complexions may be different, though, owing to the associated differences in structure and distortion of the underlying lattice defects. The discovery of linear complexions provides opportunities to nanostructure alloys via targeted segregation and confined structural states of dislocations.

#### REFERENCES AND NOTES

- P. Lejcek, *Grain Boundary Segregation in Metals* (Springer, Berlin, Heidelberg, 2010).
- I. J. Langmuir, *Am. Chem. Soc.* **40**, 1361–1403 (1918).
- M. P. Seah, *Surf. Sci.* **53**, 168–212 (1975).
- D. McLean, *Grain Boundaries in Metals* (Oxford Univ. Press, Oxford, UK, 1957).
- R. Kirchheim, *Acta Mater.* **55**, 5129–5138 (2007).
- D. Raabe et al., *Acta Mater.* **61**, 6132–6152 (2013).
- D. Raabe et al., *Curr. Opin. Solid State Mater. Sci.* **18**, 253–261 (2014).
- M. Tang, W. C. Carter, R. M. Cannon, *Phys. Rev. Lett.* **97**, 075502 (2006).
- M. Tang, W. C. Carter, R. M. Cannon, *Phys. Rev. B* **73**, 024102 (2006).
- S. J. Dillon, M. Harmer, *Acta Mater.* **55**, 5247–5254 (2007).
- S. J. Dillon, M. Tang, W. C. Carter, M. P. Harmer, *Acta Mater.* **55**, 6208–6218 (2007).
- M. P. Harmer, *Science* **332**, 182–183 (2011).
- M. Baram, D. Chatain, W. D. Kaplan, *Science* **332**, 206–209 (2011).
- W. Kaplan, D. Chatain, P. Wynblatt, W. C. Carter, *J. Mater. Sci.* **48**, 5681–5717 (2013).
- T. Frolov, D. L. Olmsted, M. Asta, Y. Mishin, *Nat. Commun.* **4**, 1899 (2013).
- T. Frolov, S. V. Divinski, M. Asta, Y. Mishin, *Phys. Rev. Lett.* **110**, 255502 (2013).
- P. R. Cantwell et al., *Acta Mater.* **62**, 1–48 (2014).
- Materials and methods are available as supplementary materials on Science Online

- M. Herbig et al., *Phys. Rev. Lett.* **112**, 126103 (2014).
- W. Guo et al., *Phys. Rev. Lett.* **113**, 035501 (2014).
- M. Herbig, P. Choi, D. Raabe, *Ultramicroscopy* **153**, 32–39 (2015).

- L. Rigutti et al., *Nano Lett.* **14**, 107–114 (2014).
- I. Arslan, E. A. Marquis, M. Homer, M. A. Hekmaty, N. C. Bartelt, *Ultramicroscopy* **108**, 1579–1585 (2008).
- O. C. Hellman, J. A. Vandenbroucke, J. Rüsing, D. Isheim, D. N. Seidman, *Microsc. Microanal.* **6**, 437–444 (2000).
- J. W. Cahn, *Acta Metall.* **5**, 169–172 (1957).
- K. E. Easterling, A. R. Thölen, *Acta Metall.* **24**, 333–341 (1975).
- R. Bullough, B. A. Bilby, *Proc. Phys. Soc. B* **69**, 1276–1286 (1956).
- T. Furuhashi, T. Maki, *Mater. Sci. Eng. A* **312**, 145–154 (2001).
- Thermo-Calc Software AB, TCFE7\_TCS steels/Fe-Alloys Database, Version 7.1 (Thermo-Calc Software AB, Stockholm).
- N. Nakada, T. Tsuchiyama, S. Takaki, N. Miyano, *ISIJ Int.* **51**, 299–304 (2011).
- S. Nag et al., *Acta Mater.* **60**, 6247–6256 (2012).

#### ACKNOWLEDGMENTS

The authors gratefully acknowledge funding by the European Union, provided under the 7th Framework Programme through the European Research Council Advanced Grant SMARTMET. M.H. is grateful to the German Research Foundation [Deutsche Forschungsgemeinschaft (DFG)] for funding through SFB 761 “Steel Ab Initio.” Data are available in the main text and the supplementary materials.

#### SUPPLEMENTARY MATERIALS

www.sciencemag.org/content/349/6252/1080/suppl/DC1  
Materials and Methods  
Figs. S1 and S2  
Table S1

1 April 2015; accepted 8 July 2015  
10.1126/science.aab2633

#### MATERIALS SCIENCE

# Highly thermally conductive and mechanically strong graphene fibers

Guoqing Xin,<sup>1</sup> Tiankai Yao,<sup>1</sup> Hongtao Sun,<sup>1</sup> Spencer Michael Scott,<sup>1</sup> Dali Shao,<sup>2</sup> Gongkai Wang,<sup>1</sup> Jie Lian<sup>1\*</sup>

Graphene, a single layer of carbon atoms bonded in a hexagonal lattice, is the thinnest, strongest, and stiffest known material and an excellent conductor of heat and electricity. However, these superior properties have yet to be realized for graphene-derived macroscopic structures such as graphene fibers. We report the fabrication of graphene fibers with high thermal and electrical conductivity and enhanced mechanical strength. The inner fiber structure consists of large-sized graphene sheets forming a highly ordered arrangement intercalated with small-sized graphene sheets filling the space and microvoids. The graphene fibers exhibit a submicrometer crystallite domain size through high-temperature treatment, achieving an enhanced thermal conductivity up to 1290 watts per meter per kelvin. The tensile strength of the graphene fiber reaches 1080 megapascals.

As one of carbon’s allotropes, single-layer graphene has the highest thermal conductivity ever reported, up to  $\sim 5000 \text{ W m}^{-1} \text{ K}^{-1}$  at room temperature (1–3); it also has the highest Young’s modulus ( $\sim 1100 \text{ GPa}$ ) (4), fracture strength (130 GPa) (4), and mobility of

charge carriers ( $200,000 \text{ cm}^2 \text{ V}^{-1} \text{ s}^{-1}$ ) (5). However, such remarkable properties of single-layer graphene are on a molecular level and have not been achieved when processed into fibers. Macroscopic graphene oxide (GO) fibers can be assembled from a dispersion of GO in aqueous media, with graphene fibers produced upon reduction of the GO fibers (6, 7). The anisotropic liquid crystalline behavior of the GO sheets can lead to a prealigned orientation, which can further be directed under shear flow to form an ordered assembly in a macroscopic fiber structure

<sup>1</sup>Department of Mechanical, Aerospace and Nuclear Engineering, Rensselaer Polytechnic Institute, 110, 8th Street, Troy, NY 12180, USA. <sup>2</sup>Department of Electrical, Computer, and Systems Engineering, Rensselaer Polytechnic Institute, 110, 8th Street, Troy, NY 12180, USA.

\*Corresponding author. E-mail: lian@rpi.edu